Molecular dynamics simulation of effective thermal conductivity of vapor-filled nanogap and nanocavity

G. S. Hwang and M. Kaviany[a)]
Department of Mechanical Engineering, University of Michigan, Ann Arbor, Michigan 48109, USA

(Received 27 April 2009; accepted 27 June 2009; published online 31 July 2009)

The effect of adsorption on momentum a_u and thermal a_T accommodation coefficients and effective thermal conductivity $\langle k_f \rangle$ of Ar vapor-filled Pt nanogap and nanocavity is examined using nonequilibrium molecular dynamics (MD) simulations. For the accommodation coefficients, the increase in solid-fluid or fluid-fluid interatomic interactions within adsorbed layer causes transitions in magnitudes of a_u and a_T near Ar triple-point temperature. In the nanogap, $\langle k_f \rangle$ MD results are in close agreement with the available closed-form solution for transition-flow regime, i.e., Knudsen number $0.1 < \mathrm{Kn}_L < 10$, using the MD results of a_T. In the nanocavity, the adiabatic sidewalls do not significantly alter the gas mean free path and $\langle k_f \rangle$, and the sparse adsorption coverage on the sidewalls results in a negligibly small fluid circulation by surface diffusion under a temperature gradient. © *2009 American Institute of Physics*. [DOI: 10.1063/1.3186043]

I. INTRODUCTION

When gas is confined in spacing with a characteristic length L comparable or smaller than its mean free path λ_f (average traveled distance without collision with adjacent particles), the effective thermal conductivity of the gas $\langle k_f \rangle$ is reduced due to the interaction of the gas particles with the confining surfaces.[1–3]

In nonconfined gas (continuum regime, $\mathrm{Kn}_L < 0.001$, Knudsen number $\mathrm{Kn}_L \equiv \lambda_f / L$), thermal conductivity is related to a number density of fluid particles n_f, specific heat capacity $c_{v,f}$, mean thermal velocity $\langle u_f \rangle$, and λ_f [1,4,5] as

$$k_f = \tfrac{5}{4} n_f c_{v,f} \langle u_f \rangle \lambda_f. \tag{1}$$

However, in the severely confined gas (free-molecular regime, $\mathrm{Kn}_L > 10$), the effective thermal conductivity $\langle k_{f,fm} \rangle$ is[1]

$$\frac{\langle k_{f,fm} \rangle}{L_z} = \frac{p_g (c_{v,f} + R_g/2)}{\dfrac{1}{a_{T,1}} + \dfrac{1}{a_{T,2}} - 1} \frac{1}{(2\pi M R_g T_g)^{1/2}}, \tag{2}$$

where L_z is the gap size along the z direction (it is used for Kn_L), p_g is the gas pressure, R_g is the ideal gas constant, M is the gas molecular weight, T_g is the gas temperature, $a_{T,1}$ and $a_{T,2}$ are the thermal accommodation coefficients for two confining surfaces. In moderately confined gas (transition regime, $0.1 < \mathrm{Kn}_L < 10$), the effective thermal conductivity $\langle k_{f,t} \rangle$ is[2,3]

$$\langle k_{f,t} \rangle = \langle k_{f,fm} \rangle \left(1 + \frac{4}{15} \frac{1}{\mathrm{Kn}_L} \frac{a_{T,1} a_{T,2}}{a_{T,1} + a_{T,2} - a_{T,1} a_{T,2}} \right)^{-1}. \tag{3}$$

The thermal accommodation coefficient for monatomic gas is[6]

$$a_T \equiv \frac{\langle T_f \rangle - \langle T_f \rangle'}{\langle T_f \rangle - \langle T_s \rangle}. \tag{4}$$

where $\langle T_f \rangle$ and $\langle T_f \rangle'$ are the temperatures of incident and reflected particles, respectively, and $\langle T_s \rangle$ is the solid surface temperature. When $a_T = 1$, fluid particles are completely accommodated with the solid surface (i.e., particle reflects with the surface temperature). Similarly, the tangential momentum accommodation coefficient is[1]

$$a_u \equiv \frac{\langle u_{f,x} \rangle - \langle u_{f,x} \rangle'}{\langle u_{f,x} \rangle}. \tag{5}$$

where $\langle u_{f,x} \rangle$ and $\langle u_{f,x} \rangle'$ are the tangential components of incident and reflected particles, respectively.

Near the saturation temperature, condensable gas adsorbs onto confining surface by interatomic/molecular potential and this adsorbed layer enhances thermal a_T and momentum a_u accommodation coefficients due to an increase in the fluid particle-confining surface interactions. This increased thermal accommodation, in turn, enhances the effective thermal conductivity, and the larger momentum accommodation increases viscous shear stress at the confining surface. This adsorption-affected heat transfer is significant in gas-filled nanopores, such as thermal insulation aerogels[7,8] and polymer electrolyte of fuel cells,[9,10] where the effective thermal conductivity and accommodation coefficients must be addressed. However, the effect of adsorption had not been addressed in the derivation of the closed-form solutions of the effective thermal conductivities in the molecular- and transition-flow regimes [Eqs. (2) and (3)] (Refs. 1–3) and in the treatment of the momentum[11–13] and thermal[6,12–14] accommodation coefficients.

Here we examine the effects of adsorption on the momentum a_u, thermal a_T, and effective thermal conductivity $\langle k_f \rangle$ of Ar vapor-filled Pt nanogaps and nanocavities (nanogaps with enclosing adiabatic sidewalls) using a nonequilibrium molecular dynamics (MD) simulation and in temperature and pressure ranges which include the triple point.

[a)]Electronic mail: kaviany@umich.edu.

TABLE I. Surface and gas temperatures and Knudsen number for MD simulation results presented in Figs. 2–4.

$\langle T_g \rangle$ (K)	T_h (K)	T_c (K)	Kn_L (N_f=600)	Kn_L (N_f=900)
1260	1320	1200	0.164	0.109
630	660	600	0.166	0.110
315	330	300	···	0.113
155	160	150	0.170	0.136
130	135	125	0.181	0.168
105	110	100	0.233	0.327
90	95	85	0.712	0.890
85	90	80	1.23	···

II. MD SIMULATIONS

The simulation box size is $7.8 \times 6.8 \times 20$ nm^3, and for the nanogap, periodic boundary conditions are used for the x and y directions. The Newton equation of motion is integrated by the Verlet algorithm with a time step of Δt=2 fs, and the initial temperature is controlled using the direct scaling method.[15,16] For the Ar–Ar interactions, the Lennard-Jones potential is used

$$\varphi_{ij}(r) = 4\epsilon_{ij}\left[\left(\frac{\sigma_{ij}}{r}\right)^{12} - \left(\frac{\sigma_{ij}}{r}\right)^{6}\right], \tag{6}$$

where the ϵ_{ff}=10.42 meV, the σ_{ff}=0.3405 nm, and the cutoff distance is $3.5\sigma_{ff}$.[17,18] The mass of Ar atom is $m_f = 6.636 \times 10^{-2}$ yg, and N_f=100–1536 Ar atoms are used in the simulations.

For the confining surfaces, a three-layered face-centered-cubic (111) plane solid Pt is modeled using the harmonic potential with N_s=3136 atoms. The solid temperatures are controlled using the Langevin thermostat with phantom molecules as described in Refs. 17–19. The parameters are the force constant Γ=46.8 N/m, the mass of Pt is $m_s = 3.24 \times 10^{-1}$ yg, the equilibrium distance (distance to the neighboring atoms) r_o=0.28 nm, the friction (damping) coefficient $\gamma = 5.184 \times 10^{-12}$ kg/s, and the random excitation force of the Gaussian distribution with the standard deviation $\sigma_F = (2\gamma k_B T_s/\Delta t)^{1/2}$. The temperature difference between the two surfaces is from 10 to 120 K for the accommodation coefficients (so it is larger than the temperature fluctuation of the solid), while 10 K is used for the effective thermal conductivity calculations. The temperatures and magnitudes of Kn_L for MD simulations are summarized in Table I.

For the Ar–Pt interactions, Lennard-Jones potential [Eq. (6)] is used in the nanogap, whereas a one-dimensional potential between Ar and the adiabatic sidewalls is used in the nanocavity. This is[18,19]

$$\varphi_{sf}(l) = \frac{4\pi 3^{1/2}\epsilon_{sf}}{15}\left(\frac{\sigma_{sf}}{r_o}\right)^2\left[2\left(\frac{\sigma_{sf}}{l}\right)^{10} - 5\left(\frac{\sigma_{sf}}{l}\right)^{4}\right], \tag{7}$$

where ϵ_{sf}=6.82 meV,[12] σ_{sf}=0.309 nm,[18] l is the distance between the fluid particles and sidewalls, and the cutoff distance is $3.5\sigma_{sf}$. To reach steady state, 5×10^6 time steps are simulated, then we calculate ensemble-averaged thermodynamic properties, a_u, a_T, and $\langle k_f \rangle$ over another 5×10^6 time steps. The gas pressure is calculated using the ideal gas law.

The accommodation coefficients are evaluated using Eqs. (4) and (5), following the recipes described in Refs. 12 and 13. An imaginary line is used to separate incident and reflecting particles, and is placed at the cutoff distance of the solid-fluid interaction (1 nm from the surface). The selection of distance is based on two requirements.[12,13] One is that the reflected particles must not be interfered with surface forces, and the other is that the reflected particles should not collide with the adjacent fluid particles before passing through this imaginary line. For $N_f > 1000$, the second requirement is violated due to small mean free path ($\lambda_f \sim 2$ nm). Thus, we use N_f=1536 only near the triple-point temperature, where adsorption significantly reduces the number of gaseous particles (to about 100).

The ensemble-averaged heat flux is calculated using[18,20]

$$\langle q_{k,g} \rangle = \frac{1}{V}\left[\sum_i \frac{1}{2} m_i (\mathbf{u}_i \cdot \mathbf{u}_i) u_{i,z} + \sum_i \varphi_i u_{i,z} + \frac{1}{2}\sum_i \sum_j z_{ij}(\mathbf{u}_i \cdot \mathbf{F}_{ij})\right], \tag{8}$$

where V is the volume, m_i is the mass of particle i, $\mathbf{u}_i$ is the velocity, $u_{i,z}$ is the z-component of the velocity, φ_i is the potential energy, z_{ij} is the z-component of the displacement separation, and F_{ij} is the interaction force between i and j particles. Note that $\langle\ \rangle$ represents the ensemble average. Then, the effective thermal conductivity is evaluated from the Fourier law, $\langle k_f \rangle = -\langle q_{k,g} \rangle / (\partial T/\partial z)$. Note that $\langle q_{k,g} \rangle$ is the same as the heat flowing into the hot and leaving the cold surface $\langle q_{k,s} \rangle$, which are calculated integrating the net damping and random forces with respect to time in the Langevin equation. Radiation heat transfer is neglected among the walls.

III. RESULTS AND DISCUSSIONS

A. Momentum and thermal accommodation coefficients

A snapshot of MD simulation in the nanogap, including adsorption, at $\langle T_g \rangle$=85 K with N_f=600, is shown in Figs. 1(a) and 1(b). The cold surface is below the triple-point temperature [T_{tp}=85 K (Ref. 21)], T_c=80 K, whereas the hot surface is above it, T_h=90 K. Noting that the triple-point temperature of Ar confined in Vycor glass nanopore is only 2 K larger than that for the bulk Ar,[21] thus we expect the equilibrium phase diagram of the confined Ar to be different. Here we only use the bulk triple-point temperature as a reference when addressing phase change in the Ar–Pt nanogap. Near surfaces, thermodynamic equilibrium (chemical potential) between gas and adsorbed phase determines the surface coverage. Figure 2 shows MD adsorption results, the variation in the number of adsorbed Ar atoms per unit surface area with respect to the surface temperature, $85 < T < 1320$ K, i.e., $0.06 < \epsilon_{sf}/k_B T < 0.931$. A full surface coverage by a monolayer is also marked. Note that the surface temperature ranges from the triple-point temperature to above the critical-point temperature of Ar, where $\epsilon_{sf}/k_B T_c = 0.525$ at the critical-point temperature of Ar, and $\epsilon_{sf}/k_B T_{tp} = 0.931$ at the triple-point temperature. Minor adsorption is found at high

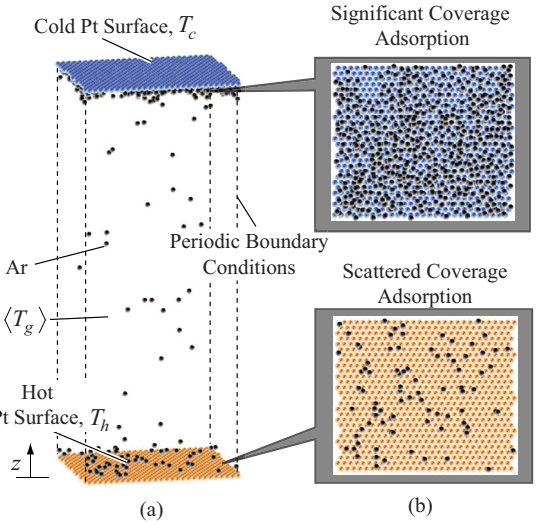

FIG. 1. (Color online) (a) Three-dimensional (3D) snapshot of simulated Ar atoms (N_f=600, Kn_L=2.1) in the nanogap at $\langle T_g \rangle$=85 K showing larger adsorption on the top cold surface and (b) stereoview of the top and bottom surfaces showing larger adsorption at the cold surface.

temperatures due to large kinetic energy compared with surface force, with an exponential increase with decreasing temperature due to a decrease in kinetic energy compared to surface force (similar to type III isobar[22]). This is associated with a relatively weak fluid-solid interatomic interaction.[22] This weak interaction results in a small decrease in the adsorption at high temperatures; however, once fluid particles adsorb onto the surface, interatomic interactions (potential) promote further adsorption. This is more pronounced at high pressure, N_f=900. A transition occurs at $\epsilon_{sf}/k_BT \simeq 0.7$ for N_f=600, whereas at $\epsilon_{sf}/k_BT \simeq 0.6$ for N_f=900. This transition, in turn, affects the accommodation coefficients and the effective thermal conductivity. Near the triple-point temperature, a fully covered adsorbed layer is found. For N_f=900, the number of adsorbed atoms continue to decrease as the

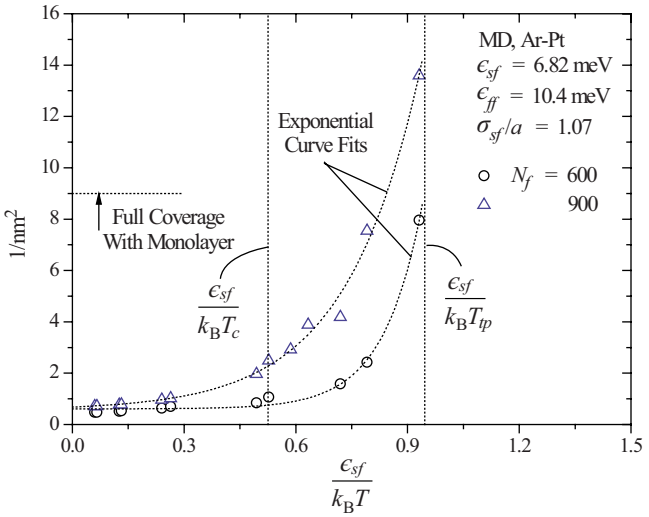

FIG. 2. (Color online) MD results showing variation in the number of adsorbed Ar atoms per unit surface area in the nanogap for N_f=600 and 900, as a function of dimensionless inverse temperature ϵ_{sf}/k_BT. Exponential curve fits to the MD results are also shown. The full surface coverage by a monolayer is also marked.

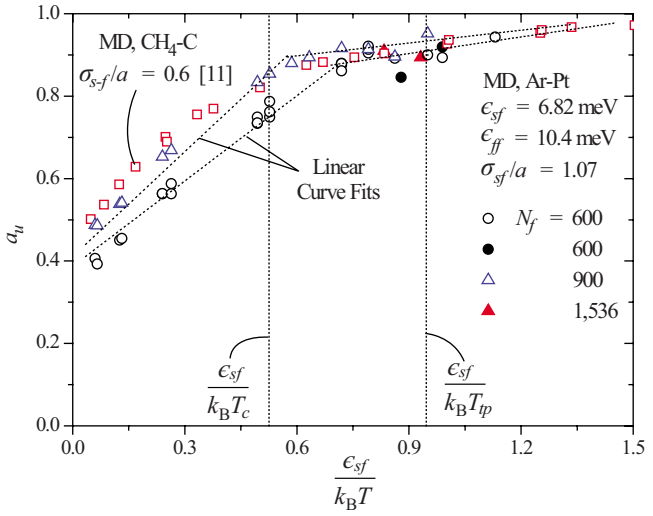

FIG. 3. (Color online) Predicted momentum accommodation coefficient a_u using N_f=600, 900, or 1536 as a function of dimensionless inverse temperature ϵ_{sf}/k_BT, showing transitions at ϵ_{sf}/k_BT=0.7 for N_f=600 and ϵ_{sf}/k_BT=0.6 for N_f=900. For N_f=600, solid circles are the MD results for the hot surface above the triple-point temperature and the cold surface below it. Other simulation results are shown Ref. 11. The linear curve fits, critical-, and triple-point temperatures of Ar are also shown.

temperature increases, whereas for N_f=600, those are nearly constant above the critical temperature. This residual adsorption at high pressures leads to pressure-dependent a_u and a_T but is expected to disappear at very high temperature (large gas superheat). Note that Kn_L changes with adsorption as shown in Table I.

Adsorption influences the surface momentum and energy exchange as manifested through a_u and thermal a_T accommodation coefficients. In Figs. 3 and 4, variations in MD simulated a_u and a_T are shown with respect to surface temperatures, $75 < T < 1320$ K, i.e., $0.06 < \epsilon_{sf}/k_BT < 1.13$. a_u has a low value $a_u \simeq 0.33$ at high temperature $\epsilon_{sf}/k_BT \to 0$,

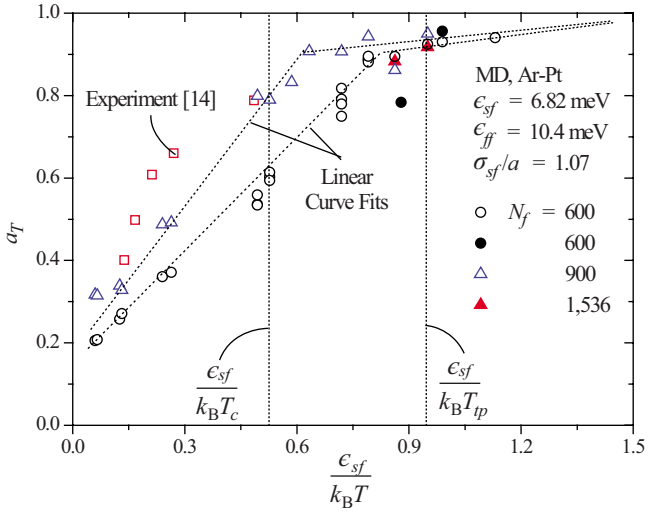

FIG. 4. (Color online) Predicted thermal accommodation coefficient a_T using N_f=600, 900, or 1536 as a function of dimensionless inverse temperature ϵ_{sf}/k_BT, showing transitions at ϵ_{sf}/k_BT=0.7 for N_f=600 and ϵ_{sf}/k_BT=0.6 for N_f=900. For N_f=600, solid circles represent the simulation results for the hot surface above the triple-point temperature and the cold surface below it. Experimental results are shown (Ref. 14). The linear curve fits, critical-, and triple-point temperatures of Ar are also shown.

and increases toward unity (diffuse and no temperature slip) with decreasing temperature $\epsilon_{sf}/k_BT \to \infty$. At low temperature, the kinetic energies of incident particles are small enough for significant solid-fluid interactions (adsorption), i.e., the adsorbed particles fluctuate several times due to the attractive surface force before escaping out of the potential well. In addition, the adsorbed particles exchange kinetic energies with the neighboring adsorbed particles. These cause the increased a_u and result in the transition at $\epsilon_{sf}/k_BT \simeq 0.7$. This is related to the temperature where significant adsorption disappears. At high temperatures (above the critical point), incident particles have dominant kinetic energy (over solid-fluid potential energy) and reflect without significant accommodation. In addition, this transition appears even at low temperatures, $\epsilon_{sf}/k_BT \simeq 0.931$, i.e., the hot surface is set above the triple-point temperature and the cold is below it, as marked with a solid circle in Fig. 3 (the simulated snapshot is also shown in Fig. 1). A fully covered adsorption layer is found at the cold surface, which, in turn, results in large a_u (also shown in Fig. 2), whereas the sparse coverage at the hot surface leads to small a_u. In addition, the simulated results at high pressure, N_f=900 show increased a_u compared to N_f =600, with nearly 30% increased surface adsorbed layer coverage at high temperatures, whereas a_u values are nearly the same results for N_f=600 and 1536 due to a full coverage at low temperatures, as shown in Fig. 2. The transition point also shifts toward higher temperature $\epsilon_{sf}/k_BT \simeq 0.6$, due to the increase in a surface coverage. The magnitudes of a_u for monatomic gases are found to be nearly independent of the pressure at high temperatures from a number of experiments.[23] This is related to rough surfaces where a relatively larger adsorption is observed. We use ideal (smooth) solid surfaces, and this may cause a pressure dependence in the temperature range considered.

The MD results are compared to other available MD results,[11] and a difference is found especially at high temperatures. This is related to the increased effective solid-fluid potential due to a rough surface (larger adsorption), as discussed in Ref. 11 (σ_{sf}/a, where σ_{sf} is the separation constant between the solid and the fluid and a is the lattice constant of the solid). Note that in Ref. 11 a rough surface (σ_{sf}/a=0.6) is modeled compared to the surface in this study (σ_{sf}/a =1.07), which provides a large effective solid-fluid interaction potential (larger solid surface area). This, in turn, results in larger adsorption and larger a_u. This causes transition even at higher temperatures (above $\epsilon_{sf}/k_BT \simeq 0.3$).

Adsorption-affected transition is also found in MD results for the thermal accommodation coefficient a_T and is more pronounced at $\epsilon_{sf}/k_BT \simeq 0.7$ and $\epsilon_{sf}/k_BT \simeq 0.931$. Moderate pressure dependence of a_T, N_f=900 (due to nearly 30% increased adsorption surface coverage) is also found at high temperature, whereas no pressure dependence appears at low pressure (due to nearly full adsorption coverage), as shown in Fig. 2. The pressure dependency of a_u at high temperatures is expected to disappear at very large temperatures. This is because a_T is evaluated using normal and tangential velocity components [Eq. (4)], whereas a_u uses only the tangential velocity components [Eq. (5)]. The MD results are also compared to the available experiment at the high temperatures,[14] and a moderate agreement is found. This difference is related to the significant adsorbed layer caused by the rough or contaminated surface in the experiment. Eventually, it is expected to disappear at high temperatures $\epsilon_{sf}/k_BT \to 0$, i.e., no adsorption. In the experiment, there is also a transition at $\epsilon_{sf}/k_BT \simeq 0.3$.

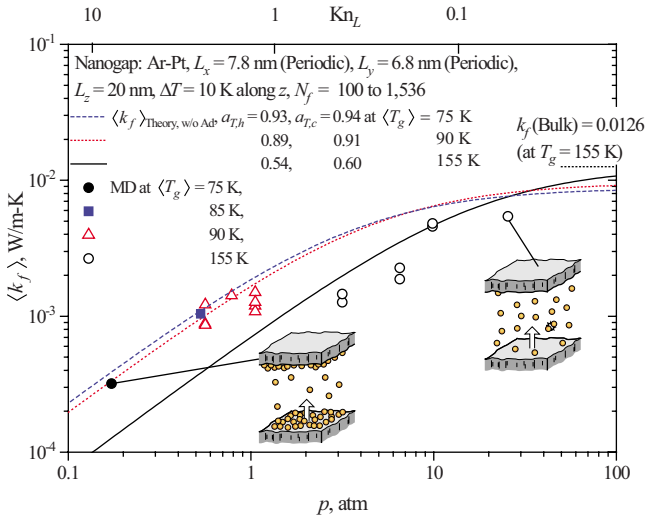

FIG. 5. (Color online) MD results for the effective thermal conductivity $\langle k_f \rangle$ in the nanogap with respect to vapor pressure $\langle p_g \rangle$ and Kn$_L$ at a few vapor temperatures $\langle T_g \rangle$. Comparisons with the the available closed-form solution [Eq. (3)] using predicted a_T are shown. The thermal conductivity of nonconfined (bulk) vapor k_f [Eq. (1)] is also shown.

B. Effective thermal conductivity in the nanogap and nanocavity

In the nanogap, the effective thermal conductivity in the transition regime is calculated between the triple-point and the critical-point temperatures and is compared to Eq. (3) using the predicted a_T, as shown in Fig. 5. Overall, the MD results are in good agreement with that solution within 20% uncertainty even at low temperatures (significant adsorption). Note that Eq. (3) had been derived using the Maxwell integral equations of transfer, the Maxwell velocity distribution function of fluid particles, and the gas temperatures near the confining surfaces (predicted by the accommodation coefficients and confining surface temperatures, neglecting adsorption) as the boundary conditions. This approach is still valid even with adsorption since the thermal accommodation coefficients account for the effective fluid-wall molecular interactions. The MD results show that high temperatures allow for a large number density of gaseous particles, n_f (small Kn$_L$) without significant adsorption and large mean thermal velocity, which increase $\langle k_f \rangle$. However, the absence of adsorption results in low a_T, limiting $\langle k_f \rangle$. At low temperatures, small kinetic energy leads to significant adsorption, which, in turn, increases $\langle k_f \rangle$ by increasing a_T, whereas it causes large Kn$_L$ and small mean thermal velocity which reduces $\langle k_f \rangle$. The calculated $\langle k_f \rangle$ is smaller than the bulk k_f [Eq. (1)] due to large Kn$_L$ and small a_T.

In the nanocavity, a snapshot of MD simulation, at $\langle T_g \rangle$=90 K with N_f=600, is shown in Figs. 6(a) and 6(b). The nanocavity creates significant adsorption around the cor-

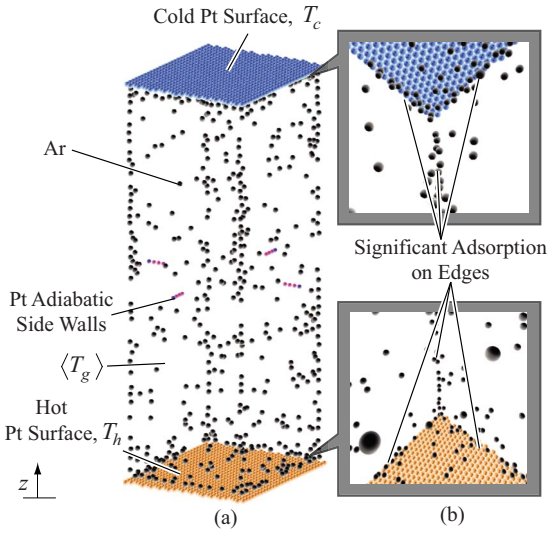

FIG. 6. (Color online) (a) 3D snapshot of simulated Ar atoms (N_f=600, Kn_L=0.73) in the nanocavity at $\langle T_g \rangle$=90 K and (b) stereoview of top and bottom corners showing larger adsorption at the edges and corners.

ners where the surface forces overlap, which, in turn, results in scattered adsorption on the hot, cold, and sidewall surfaces. In Fig. 7, a reasonable agreement is also found between the MD results and Eq. (3), even at low temperatures (close to the triple-point temperature). The adiabatic sidewalls do not significantly influence the mean free path due to the elastic collisions between the fluid particles and sidewalls. In addition, a significant adsorption is found around the edges (corners) of sidewalls, where the surface forces overlap, as shown in Figs. 6(a) and 6(b). However, due to scattered, partial coverage, this is not sufficient enough to produce significant surface diffusion along the sidewalls and a circulation within the cavity under a temperature gradient.

IV. CONCLUSIONS

For the transition-flow regime ($0.1 < \mathrm{Kn}_L < 10$), momentum a_u and thermal a_T accommodation coefficients, and effective thermal conductivity $\langle k_f \rangle$ are calculated for Ar vapor filled in the Pt nanogap and nanocavity using nonequilibrium MD simulation over triple-to critical-point temperature range. This allows for examining the effect of adsorption on the surface interaction kinetics as well as the gaseous thermal transport.

For a_u and a_T, we find transition at near triple point, $\epsilon_{s\text{-}f}/k_B T \simeq 0.7$ for N_f=600 and $\epsilon_{s\text{-}f}/k_B T \simeq 0.6$ for N_f=900, while it varies with the solid surface roughness and surface coverage by adsorption. These coefficients increase with decreasing temperature and eventually reach unity. This transition is caused by adsorption, i.e., increased solid-fluid and fluid-fluid interactions within the adsorbed layer. This transition also depends on the pressure. Larger accommodation coefficients are also found at high pressures, where significant adsorption occurs. The adsorption-affected transition is more pronounced in a_T because a_T is evaluated using both normal and tangential velocity components, whereas a_u uses only the tangential velocity components.

In the nanogap, the MD results for the effective thermal conductivity are in agreement with the available closed-form solution for the transitional-flow regime.[2,3] This agreement extends even in the presence of adsorption at low temperatures.

In the nanocavity, the calculated thermal conductivity is nearly the same as that of the nanogap since the adiabatic sidewalls do not significantly alter the fluid particle mean free path, i.e., because of the elastic collision with the wall. In addition, adsorption occurs mainly around the edges where the surface forces overlap, which, in turn, leads to dispersed adsorption on the hot and cold, sidewall surfaces. This does not produce significant surface diffusion for the surface return of the particles along the adiabatic sidewalls. Thus, any circulation with the nanocavity under a temperature gradient would require very high pressure and low temperature for significant adsorption coverage.

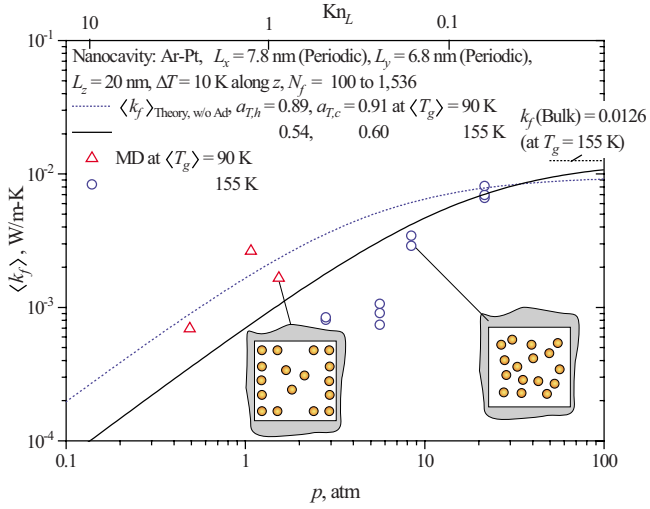

FIG. 7. (Color online) MD results for the effective thermal conductivity $\langle k_f \rangle$ in the nanocavity as a function of vapor pressure $\langle p_g \rangle$ and Kn_L, at a few vapor temperatures $\langle T_g \rangle$. Comparisons with the available closed-form solution [Eq. (3)] using predicted a_T are shown. The thermal conductivity of nonconfined (bulk) vapor k_f is also shown.

ACKNOWLEDGMENTS

We would like to thank Professor Maruyama and Professor Shiomi for useful discussions on the MD simulation of the Langevin thermostat and Professor Ohara for valuable communications on the calculation of energy exchange at the interface.

[1] E. Kennard, *Kinetic Theory of Gases* (McGraw-Hill, New York, 1938).
[2] C. Y. Liu and L. Lees, "Kinetic Theory Description of Plane Compressible Couette Flow," in *Rarefied Gas Dynamics*, edited by L. Talbot (Academic Press, New York, 1961), pp. 391–428.
[3] G. S. Springer, "Heat Transfer in Rarefied Gases," in *Advances in Heat Transfer*, edited by J. P. Hartnett and T. F. Irvine, Jr. (Academic Press, New York, 1971), Vol. 7, pp. 163–218.
[4] C. Tien and J. Lienhard, *Statistical Thermodynamics* (Holt, Rinehart and Winston, New York, 1971).
[5] M. Kaviany, *Heat Transfer Physics* (Cambridge University Press, Cambridge, 2008).
[6] J. Blömer and A. Beylich, Surf. Sci. **423**, 127 (1999).
[7] L. Hrubesh and R. Pekala, J. Mater. Res. **9**, 731 (1994).
[8] J. Lou, S. Harrington, and D.-M. Zhu, Phys. Rev. E **60**, 5778 (1999).
[9] P. Costamagna, S. Grosso, and R. D. Felice, J. Power Sources **178**, 537 (2008).
[10] G. Hwang, J. Nam, M. Kim, S. Son, and M. Kaviany, J. Electrochem. Soc. (to be published).

[11]G. Arya, H. Chang, and E. McGinn, Mol. Simul. **29**, 697 (2003).
[12]P. Spijker, A. Markvoort, P. Hilbers, and S. Nedea, AIP Conf. Proc. **1084**, 659 (2008).
[13]P. Spijker, A. Markvoort, S. Nedea, and P. Hilbers, Proceedings of ICNMM, Sixth International Conference on Nanochannels, Microchannels and Minichannels, Darmstadt, Germany 2008 (unpublished), Vol. 1, p. 1.
[14]S. Borisov, S. Litvinenko, Y. Semenov, and P. Suetin, J. Eng. Phys. Thermophys. **34**, 603 (1978).
[15]M. Allen and D. Tildesley, *Computer Simulation of Liquids* (Oxford University Press, Oxford, 1989).
[16]D. Frenkel and B. Smit, *Understanding Molecular Simulation* (Academic, New York, 2002).
[17]S. Maruyama and T. Kimura, Therm. Sci. Eng. **7**, 63 (1999).
[18]C. Wang, J. Chen, J. Shiomi, and S. Maruyama, Int. J. Therm. Sci. **46**, 1203 (2007).
[19]W. J. Minkowycz, and E. M. Sparrow, eds., *Advances in Numerical Heat Transfer* (Taylor & Francis, New York, 2000), Vol. 2, Chap. 6, pp. 189–226.
[20]T. Ohara, J. Chem. Phys. **111**, 9667 (1999).
[21]D. Jones and H. Fretwell, J. Phys.: Condens. Matter **15**, 4709 (2003).
[22]S. Gregg and K. Sing, *Adsorption, Surface Area and Porosity* (Academic, London, 1982).
[23]A. Agrawal and S. Prabhu, J. Vac. Sci. Technol. A **26**, 634 (2008).